Computational Biology:

Allosteric Response and Substrate Sensitivity in Peptide Binding of the Signal Recognition Particle

Connie Y. Wang and Thomas F. Miller III

J. Biol. Chem. 2014, 289:30868-30879.
doi: 10.1074/jbc.M114.584912 originally published online September 18, 2014

THE JOURNAL OF BIOLOGICAL CHEMISTRY VOL. 289, NO. 44, pp. 30868–30879, October 31, 2014

Allosteric Response and Substrate Sensitivity in Peptide Binding of the Signal Recognition Particle

Received for publication, May 27, 2014, and in revised form, September 17, 2014 Published, JBC Papers in Press, September 18, 2014, DOI 10.1074/jbc.M114.584912

Connie Y. Wang[1] **and Thomas F. Miller III**[2]

From the Division of Chemistry and Chemical Engineering, California Institute of Technology, Pasadena, California 91106

Background: The SRP is a central component of the co-translational protein targeting pathway.
Results: Long timescale computer simulations reveal shifts in the SRP conformational distribution upon nascent protein binding.
Conclusion: The binding-induced conformational shifts correlate with the experimentally observed efficiency of protein targeting.
Significance: The work provides new insight into the mechanism by which SRP allostery regulates the fidelity of protein targeting.

We characterize the conformational dynamics and substrate selectivity of the signal recognition particle (SRP) using a thermodynamic free energy cycle approach and microsecond timescale molecular dynamics simulations. The SRP is a central component of the co-translational protein targeting machinery that binds to the N-terminal signal peptide (SP) of nascent proteins. We determined the shift in relative conformational stability of the SRP upon substrate binding to quantify allosteric coupling between SRP domains. In particular, for dipeptidyl aminopeptidase, an SP that is recognized by the SRP for co-translational targeting, it is found that substrate binding induces substantial changes in the SRP toward configurations associated with targeting of the nascent protein, and it is found that the changes are modestly enhanced by a mutation that increases the hydrophobicity of the SP. However, for alkaline phosphatase, an SP that is recognized for post-translational targeting, substrate binding induces the reverse change in the SRP conformational distribution away from targeting configurations. Microsecond timescale trajectories reveal the intrinsic flexibility of the SRP conformational landscape and provide insight into recent single molecule studies by illustrating that 10-nm lengthscale changes between FRET pairs occur via the rigid-body movement of SRP domains connected by the flexible linker region. In combination, these results provide direct evidence for the hypothesis that substrate-controlled conformational switching in the SRP provides a mechanism for discriminating between different SPs and for connecting substrate binding to downstream steps in the protein targeting pathway.

Protein targeting pathways govern the delivery of both secretory and integral membrane proteins to their appropriate cellular destinations (1). Co-translational protein targeting relies on the recognition of the N-terminal signal peptide (SP)[3] of nascent protein sequences. This process requires the signal recognition particle (SRP), a protein-RNA complex, and universally conserved component of the co-translational protein targeting machinery (2). The SRP binds to the ribosome/nascent-protein complex (RNC) and targets nascent proteins for either translocation or membrane integration via the Sec translocon (3–9).

Nascent proteins that undergo targeting via the co-translational pathway have SPs that exhibit an 8–12-residue hydrophobic core and a propensity for α-helical secondary structure (10, 11). However, the detailed mechanism by which SP binding triggers selection for co-translational targeting remains unclear. In this work, we use free energy (FE) calculations and microsecond timescale trajectories to investigate the coupling between SP binding and SRP conformational dynamics and to provide new insight into the role of SP binding in co-translational protein targeting.

Both structural (12–21) and biochemical work (22–24) suggest that the SRP exhibits multiple stable conformations that are important for protein targeting. The conserved functional core of the SRP (Fig. 1*A*) is composed of an RNA component and a multidomain protein component (25, 26). The protein component consists of a methionine-rich M domain that contains both the SP-binding site and the RNA-binding site, as well an NG domain that contains a catalytic GTPase (27–29). The M and NG domains are connected by a flexible 30-residue linker region (20). Fig. 1, *A* and *B,* represents two conformations of the SRP that have been proposed to play a central role in the initial step of SP binding to the SRP (19). Recent crystal structures reveal that although the structure of the individual domains is quite similar, the relative arrangement of the domains differs substantially between the two conformations (19, 20). Throughout this paper, we refer to these two conformations as *syn* and *anti*, indicating the relative orientation of the SRP RNA and the NG domain.

[1] Supported by National Science Foundation Graduate Research Fellowship Program Award 1144469.
[2] Supported by a Camille and Henry Dreyfus Foundation Teacher-Scholar award and an Alfred P. Sloan Foundation research fellowship. To whom correspondence should be addressed: Division of Chemistry and Chemical Engineering, California Institute of Technology, 1200 East California Blvd., Pasadena, CA. Tel.: 626-395-6588; Fax: 626-395-2031; E-mail: tfm@caltech.edu.

[3] The abbreviations used are: SP, signal peptide; SRP, signal recognition particle; RNC, ribosome/nascent-protein complex; FE, free energy; MD, molecular dynamics; FEP, free energy perturbation; LJ, Lennard-Jones; PB, Poisson-Boltzmann; DPAP, dipeptidyl aminopeptidase.

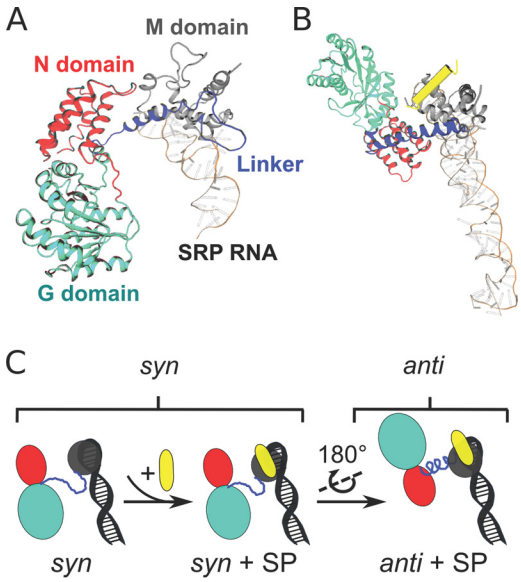

FIGURE 1. *A,* crystal structure of the *S. solfataricus* SRP in the *syn* conformation (20). A disordered linker (*blue*) region connects the N (*red*) and G (*green*) domains to the M (*gray*) domain that is bound to the SRP RNA. *B,* crystal structure of the *M. jannaschii* SRP in the *anti* conformation with bound SP (*yellow*) (19). *C,* proposed mechanism in which SP binding leads to a shift in the SRP conformational distribution from the *syn* conformation to the *anti* conformation.

Biochemical evidence suggests that SP binding influences the kinetics of downstream targeting events, such as dimerization of the SRP with its receptor, GTPase activity of the SRP, and final release of the RNC from the SRP to the translocon channel (30). Truncation or modification of the SP has additionally been shown to modulate the rate of these targeting events (31, 32), suggesting that the targeting events serve as checkpoints for different SPs that enforce fidelity of the co-translational targeting pathway (30). Furthermore, the *anti* conformation of the SRP places the universally conserved tetraloop end of its RNA in close proximity with its catalytic NG domain (19), and it has been shown that this RNA tetraloop is essential for the protein targeting step that involves complex formation between the SRP and its receptor (33–38).

The proposed model shown in Fig. 1*C* relates initial SP binding to changes in the SRP conformation, which then impact the downstream targeting events (15, 18, 19, 39–41). In this model, SP-induced shifts of the SRP to the *anti* conformation help to organize the SRP for necessary catalytic events and interactions with its receptor.

In this study, we investigate the possibility that SP binding drives conformational changes of the SRP associated with the efficiency of subsequent targeting events. A thermodynamic FE cycle is designed to calculate the shift in SRP conformational stability upon substrate binding. Thermodynamic FE cycles have long been applied to the study of biophysical systems, addressing issues that include the solvation FE for small organic molecules (42–44), binding energy for protein-ligand interactions (45–47), the relative stability of protein conformations (48), and the relative binding preference of ligands for different protein conformations (49). The thermodynamic cycle employed in this study allows us to equate the difference in binding FE of the SP to different conformations of the SRP to SRP conformational changes upon SP binding and reduces the demands of protein conformational sampling. We calculate the allosteric effect induced by SP binding for a range of experimentally studied SPs to investigate the effect of changing the SP amino acid sequence. Furthermore, we reveal details of the large scale SRP conformational rearrangements by performing several microsecond timescale (MD) trajectories. Taken together, these calculations provide insight into the sensitivity of the SRP conformational changes to the identity of the SP. In particular, the results of this study reveal that the conformational preference of the SRP for the *anti* over the *syn* conformation upon SP binding agrees with trends found in experimentally measured targeting efficiencies, suggesting that SRP conformational dynamics are substrate-specific and provide a selection mechanism of nascent proteins for the co-translational targeting pathway.

COMPUTATIONAL METHODS

Modeling for FE Calculations—Initial coordinates for the *syn* conformation of the SRP are available from the high resolution crystal structure of the archaeal *Sulfolobus solfataricus* species (Protein Data Bank code 1QZW) (20). Coordinates for the *anti* conformation of the SRP from *S. solfataricus* have not been reported in a crystallographic study, so they are instead modeled from the available *M. jannaschii* structure (Protein Data Bank code 3NDB) (19) as follows. A pairwise sequence alignment of the *S. solfataricus* and *Methanococcus jannaschii* sequences is performed using ClustalX (50) and input into MODELLER (51). The MODELLER protocol builds coordinates for the *S. solfataricus* SRP in the *anti* conformation that minimizes a set of the spatial restraints generated from the sequence alignment with the existing *M. jannaschii* structure and a set of stereochemical restraints determined from the CHARMM22 force field (52). The model coordinates are refined with conjugate gradient minimization and molecular dynamics with simulated annealing.

The FE associated with SP binding to either the *syn* and *anti* conformations of the SRP is calculated for three SPs, listed in Table 1. The first is dipeptidyl aminopeptidase B (DPAP-WT), a prototypical example of a peptide sequence that is targeted to the co-translational targeting pathway (53). The second SP, DPAP-K464L, is obtained from the DPAP-WT sequence by a single lysine-to-leucine mutation at residue 464. This mutation extends the hydrophobic region of the SP relative to the DPAP-WT. The third SP is PhoA, which is found to bind SRP *in vitro* (10), but only weakly targets proteins via the co-translational targeting pathway (30); the *in vivo* systems alternatively select PhoA for the post-translational SecB pathway (54). A crystal structure of the DPAP-WT SP bound to the *syn* conformation of the SRP is available (Protein Data Bank code 3KL4) (17) and is used to initialize coordinates for simulations of the bound DPAP-WT. The coordinates for bound DPAP-K464L are constructed via direct substitution of the leucine side chain coordinates in DPAP-WT at residue 464 with lysine coordinates, followed by steepest descent minimization to remove steric clashes (55). The coordinates for bound PhoA are constructed by sequence alignment with the DPAP-WT SP and modeled by the MODELLER protocol described previously. We note that the N-terminal end of the SP sequences are capped using a

TABLE 1
Summary of the sequences and features of studied SPs

SP	Sequence	V(Å^3)[a]	Features
DPAP-WT	GIILVLLIWGTVLLLKSIPH	3291	Efficient co-translational targeting sequence
DPAP-K464L	GIILVLLIWGTVLLLLSIPH	3178	Single-point mutation from WT
PhoA	IALALLPLLFTPVTKA	2338	Inefficient co-translational targeting sequence

[a] Excluded volume of the SP, was determined by VMD volmap (82).

neutral acetyl group, rather than a positively charged bare ammonium terminus, to account for the fact that in the experimental crystal structure (17) the N terminus of the SP sequence is bonded to additional residues that are not resolved; and for the simulations to include a bare ammonium terminus at the N-terminal end of the SP would introduce an unphysical charge at that point in the sequence.

Free Energy Sampling—We performed nine sets of calculations to determine the FE of binding for each of the three SPs to the SRP in the *syn* or *anti* conformation. For the *i*th SP, these calculations yield, $\Delta G^{(i)}_{(aq)}$, $\Delta G^{(i)}_{\mathrm{S\,(SRP)}}$, and $\Delta G^{(i)}_{\mathrm{A\,(SRP)}}$, which are, respectively, the FE of aqueous solvation for the SP, the FE associated with transferring the SP from the vacuum state to binding the solvated SRP in the *syn* conformation, and the FE associated with transferring the SP from the vacuum state to binding the solvated SRP in the *anti* conformation. These quantities are then used to compute the FE of SP binding, $\Delta G^{(i)}_{\mathrm{S/A}} = \Delta G^{(i)}_{\mathrm{S/A\,(SRP)}} - \Delta G^{(i)}_{(aq)}$. In this study, each calculation of a FE difference was performed using the FE perturbation (FEP) method in two stages.

The first stage involves "turning on" the Lennard-Jones (LJ) interactions between the SP and the remaining atoms in the system. The second stage involves turning on the electrostatic interactions between the SP and the remaining atoms. For each stage, independent sampling trajectories were performed with potential energy functions that corresponding to different values of the parameter λ, as shown in Equation 1,

$$V(\lambda) = (1 - \lambda)V_0 + \lambda V_1 \qquad \text{(Eq. 1)}$$

For the first stage, in which the LJ interactions are turned on, V_0 refers to the noninteracting state, and V_1 refers to the state with fully interacting LJ potentials. To ensure the use of smooth potential energy functions during this process (56, 57), the LJ potential energy function was turned on using a λ-dependent soft-core potential for V_1, as implemented in Gromacs 4.5.3 (58) with $\alpha = 0.5$, $\sigma = 0.3$, and $p = 1$; the full LJ potential energy function was recovered for $\lambda = 1$. For the second stage, V_0 refers to the state with only LJ interactions (*i.e.* the electrostatically noninteracting state), and V_1 refers to the state with both LJ and electrostatic interactions. The first stage utilizes 10 trajectories corresponding to evenly spaced values of λ between 0 and 0.09, 30 trajectories corresponding to evenly spaced values of λ from 0.1 to 0.245, and 76 trajectories corresponding to evenly spaced values of λ from 0.25 to 1. The second stage utilizes 91 trajectories corresponding to evenly spaced values of λ from 0 to 0.9 and 20 trajectories corresponding to evenly spaced values of λ between 0.91 and 1.

All FE calculations of SP binding to the SRP are performed on a truncated version of the SRP system that consists of the linker region and the M domain (residues 296–432); the NG domain and the RNA are removed to reduce computational cost (Fig. 2). Consideration of this truncated system is warranted by the fact that all available crystal structures indicate that the SP binding pocket is fully contained within the combined M domain and linker region (17, 19); microsecond simulations of the untruncated system are discussed below. We note that previous experimental studies have focused on the binding of SRP to the full RNC complex, whereas the current simulation only considers the binding of the SRP to the SP portion of the RNC complex; this study thus addresses only the relative impact of the SP on the conformational changes of the SRP.

A truncated octahedral simulation cell is used with periodic boundary conditions. Na^+ and Cl^- counterions are included to achieve electroneutrality of the simulation cell at an ion concentration of 100 mM. The total system size varies for the SRP in the *syn* and *anti* conformation due to different box sizes and different numbers of solvent molecules. For FE simulations of SP binding to the SRP in the *syn* conformation, the total system size is 29,287 atoms. FE simulations of the SP binding to the SRP in the *anti* conformation have a total system size of 39,482 atoms. For simulations of the SP in an aqueous environment, the total system size is 9893 atoms. In all FE calculations, we employ the AMBER03 force field (59) and the TIP3P model for water (60).

Two sets of harmonic restraints were applied to limit the sampled configuration space for the SP and SRP molecules in the FE calculations. The first set restrains the SP to the SRP, to avoid dissociation of the SP from the SRP during the course of the long sampling trajectories. Specifically, using the PLUMED plugin (61), each SP was restrained to the SRP by six harmonic restraints between the Cα atoms of residues 4, 10, 14, 16, 4, and 16 of each SP to the Cα atoms of residues Leu-428, Met-424, Glu-416, Glu-412, Ala-334, and Lys-373 of the SRP M domain, respectively; the force constant of the harmonic restraints is 55.6 kJ mol^{-1} nm^{-2}, and the distance of minimum restraint for each pairwise interaction corresponds to the crystal structure distance of the atom pair in the 3KL4 structure (17). The second set of harmonic restraints limits the ensemble of sampled configurations for the SRP to those associated with either the *syn* or *anti* structures that are observed in the experimental crystal structures (19, 20). Specifically, for both the *syn* and *anti* conformations of the SRP, each Cα atom associated with residues in the linker region of the SRP (residues 296–330) is restrained in absolute space to its corresponding position in the experimental crystal structure, using a force constant of 1000 kJ mol^{-1} nm^{-2}. For all sampling trajectories associated with a given FE calculation, the applied restraint potentials retain the same minimum and force constant, even as the other molecular interactions are alchemically modified as part of the FEP method.

For every sampling trajectory (each of which is associated with a different value of the λ parameter in one of the two stages

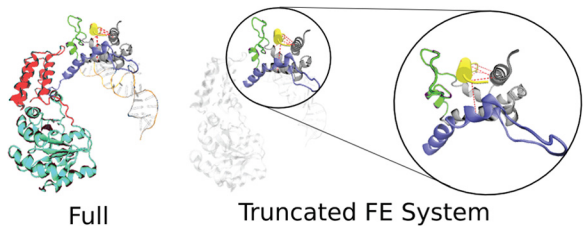

FIGURE 2. **Truncation of SRP for FE calculations.** The full SRP system includes the N domain (*red*), G domain (*green*), linker region (*blue*), and M domain (*gray*) with fingerloop (*light green*) and bound SP (*yellow*). The truncated system consists of the *circled* M domain and linker region.

of the FE calculation), the initial configuration of the system was subjected to both relaxation and equilibration before data collection. First, the steepest descent minimization (55) is performed to reduce steric clashes to a force tolerance of 100 kJ mol^{-1} nm^{-1}. Second, equilibration in the NVT ensemble is performed for 100 ps. Third, for FE calculations with the SRP, we perform 3 ns of equilibration in the NPT ensemble; for FE calculations without the SRP (*i.e.* aqueous environment), we perform 1 ns of equilibration in the NPT ensemble before data collection. Relaxation, equilibration, and sampling are done within the FEP framework implemented in the Gromacs 4.5.3 package (58). The system is evolved using Langevin dynamics with a damping constant of 1 ps^{-1} and a temperature of 300 K. The Parrinello-Rahman barostat (62) is applied for pressure coupling at 1 bar. The particle mesh Ewald method (63, 64) is used to evaluate the electrostatic interactions with a real space cutoff of 10 Å. The LJ interactions are switched off between 8 and 9 Å using a cubic spline, and a long range dispersion correction is applied to the energy and pressure during the course of the simulation to correct for the cutoff (65). The simulations are performed with a 2-fs time step with bond distances constrained using LINCS (58). For FE trajectories associated with turning on the SP interactions in the presence of the SRP, the sampling time for each trajectory ranges from 7 to 10 ns. For trajectories associated with turning on the SP interactions in the absence of SRP (*i.e.* aqueous environment), the sampling time was 4 ns. Over 12 μs of combined simulation time was performed for the FE sampling.

The Bennett acceptance ratio method (66) is used to bidirectionally weigh the collected data from trajectories sampled in the i and $i+1$ potential and to calculate $\Delta G_{i,i+1}$, the FE difference between the i and $i+1$ states. $\Delta G_{i,i+1}$ is calculated by iteratively solving Equation 2

$$e^{\beta \Delta G_{i,i+1}} = \frac{\langle f(-\beta(\Delta U_{i+1,i} - C))\rangle_{i+1}}{\langle f(\beta(\Delta U_{i,i+1} - C))\rangle_{i}} e^{(\beta C)}$$

$$f(x) = \frac{1}{1 + e^{x}} \qquad \text{(Eq. 2)}$$

$$C = \Delta G_{i,i+1} + \frac{1}{\beta} \ln \frac{N_{i+1}}{N_i}$$

where $\Delta U_{i,i+1} = U_{i+1}(x_i) - U_i(x_i)$. $U_i(x_i)$ is the potential energy of the configuration x_i sampled with the i potential and evaluated in the i potential. $U_{i+1}(x_i)$ is the potential energy of the configuration x_i sampled with the i potential but evaluated in the $i+1$ potential. N_i is the number of independently sampled points in trajectory i.

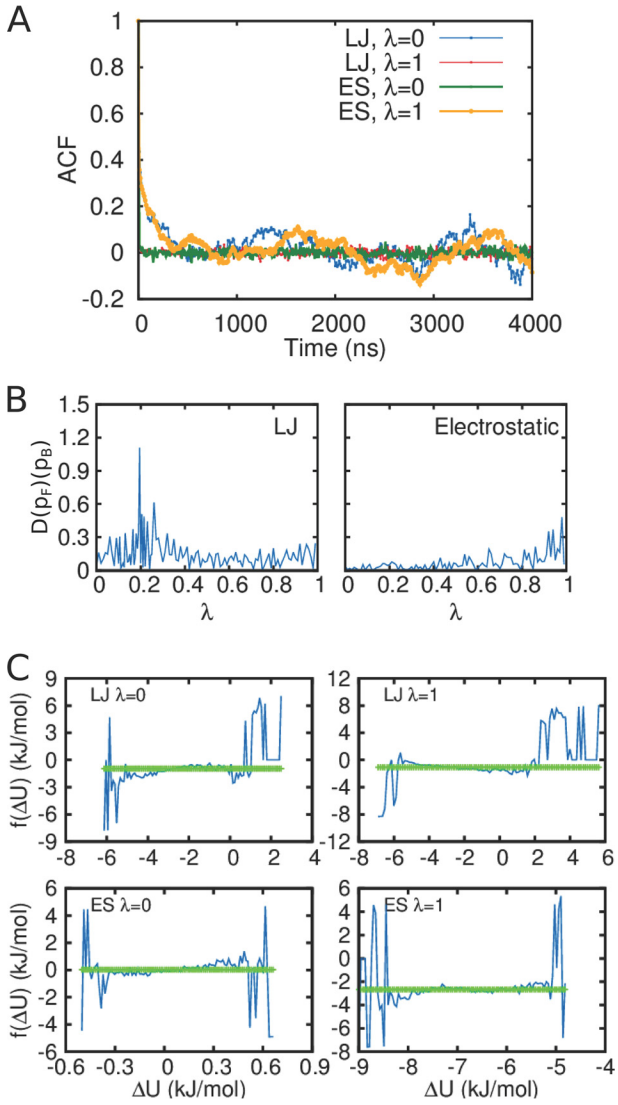

FIGURE 3. *A*, autocorrelation function (*ACF*) of representative sampling trajectories for FE simulations that illustrate decorrelation times in the range of 1–900 ns. These decorrelation estimates are used to determine the frequency of sampling. *B*, relative entropy measure, $D(p_F)(p_B)$ (Equation 3), between neighboring trajectories for FE simulations is used to determine the spacing of λ values for the LJ and electrostatic perturbations such that all neighboring trajectories have a relative entropy less than 1.5 (67). *C*, Bennett's overlapping histograms for representative $\Delta G_{i,i+1}$ in FE simulations where $f(\Delta U) = g_B(\Delta U) - g_F(\Delta U)$ is plotted in *blue* and the Bennett acceptance ratio result, $\beta\Delta G_{i,i+1}$ is plotted in *green*. For a region of overlap between the forward and backward ΔU distribution, $f(\Delta U)$ should be constant and equal to $\beta\Delta G_{i,i+1}$.

For each FE calculation, the convergence of each sampling trajectory and the overlap between neighboring trajectories were examined by plotting the autocorrelation function of $\Delta U_{i,i+1}(t)$ and the relative entropy, defined in Equation 3,

$$D(p_F)(p_B) = \int p_F \ln\left(\frac{p_F}{p_B}\right) \qquad \text{(Eq. 3)}$$

where $p_F = P(\Delta U_{i,i+1})$ and $p_B = P(\Delta U_{i,i+1})$ and where $D = 0$ for identical distributions. In Fig. 3, we show these convergence and overlap measures for the case of DPAP-WT SP bound to

SRP in the *anti* conformation, and similar results are seen for all other FE calculations in this study. In Fig. 3*A*, we find decorrelation times in the range of 1–900 ns that are used to determine the frequency of sampling for the FE calculations. In all cases, the decorrelation time for the individual trajectory is shorter than the total sampling time. The overlap between neighboring trajectories is shown in Fig. 3*B* and sufficient windows are added such that $D(p_F)(p_B) \leq 1.5$ to ensure good overlap (67).

To provide an alternative test of the overlap, we use the overlapping histogram method of Bennett (66), which plots $g_F(\Delta U) - g_B(\Delta U)$, as defined in Equation 4,

$$g_F(\Delta U) = \ln p_F(\Delta U) - \frac{1}{2}\beta\Delta U$$
$$g_B(\Delta U) = \ln p_B(\Delta U) + \frac{1}{2}\beta\Delta U \quad \text{(Eq. 4)}$$

In Fig. 3*C*, $g_B(\Delta U) - g_F(\Delta U)$ is compared with the value of $\beta\Delta G$ calculated via the Bennett acceptance ratio method. For trajectories with sufficient overlap and correct sampling, $g_B(\Delta U) - g_F(\Delta U) = \beta\Delta G$ over a range of ΔU values, where $p_F(\Delta U)$ and $p_B(\Delta U)$ have significant overlap.

Additional analysis was performed to avoid possible artifacts in the reported FE calculations due to long range electrostatics. The DPAP-WT sequence is the only SP considered in this study that involves a net charge; the SP sequences PhoA and DPAP-K464L are both neutral. Care must be taken when using the particle mesh Ewald description of long range electrostatics to calculate relative free energies that involve the manifestation of a net charge (such as $\Delta G_S^{(\text{DPAP-WT})}$ and $\Delta G_A^{(\text{DPAP-WT})}$), because calculations of this kind can be sensitive to the size of the total simulation cell (68). Although one might expect this effect to be small in simulations as large as those performed here, which range from 29,287 to 39,482 atoms in size, we have nonetheless performed two robustness tests to explicitly confirm that such system-size artifacts do not impact the results presented here. In the first robustness test, we utilize the method of Lin *et al.* (68) to compute the leading order correction to the FE differences due to long range electrostatics (Equation 22 of Ref. 68), which accounts for the shift in the electrostatic potential due to the finite system size of the simulation cell. The calculated corrections are 1.89 and 1.71 kJ/mol for $\Delta G_S^{(\text{DPAP-WT})}$ and $\Delta G_A^{(\text{DPAP-WT})}$, respectively, such that the relative shift in these quantities due to the system-size effect is only 0.18 kJ/mol; because the relative FE of SP binding to the SRP in the *syn versus* the *anti* conformation is sensitive only on this small relative shift (Equation 5), the system-size effect is concluded to be negligible. In the second robustness test, we estimate the error from the constraint imposed on the polarization of the cell as a result of periodic boundary conditions (68). Using the Delphi 4.0 (69) program, Poisson-Boltzmann (PB) continuum dielectric calculations were performed to estimate the electrostatic FE both with and without periodic boundary conditions. The calculated corrections are 0.26 and 0.22 kJ/mol for $\Delta G_S^{(\text{DPAP-WT})}$ and $\Delta G_S^{(\text{DPAP-WT})}$, respectively, such that the relative shift in these quantities due to the system-size effect is only 0.04 kJ/mol. Again, because the relative FE of SP binding to the SRP in the *syn versus* the *anti* conformation is sensitive only on this small relative shift, the system-size effect associated with the polarization constraint is concluded to be negligible. In summary, the results from both tests suggest that the conclusions drawn in this paper are robust with respect to possible system-size effects associated with long range electrostatics.

Microsecond Timescale Trajectories of the Untruncated SRP—Microsecond timescale trajectories of the SRP system are performed on the Anton supercomputer, a special-purpose machine for long timescale MD simulations (70, 71). Unlike the FE calculations, the Anton trajectories were performed without any truncation of the SRP system; the simulations included the full RNA, M, and NG domains of the SRP. Four trajectories are performed as summarized in Table 3. Trajectory 1, in which the SRP is initialized from the *syn* conformation without a bound SP, is prepared with coordinates from the 1QZW structure (20). Trajectory 2, in which the SRP is initialized from the *syn* conformation with a bound DPAP-WT SP, is prepared with coordinates from the 3KL4 structure (17). Trajectory 3, in which the SRP is initialized from the *anti* conformation without a bound SP, is prepared with coordinates from the 3NDB structure (19) after removal of the model SP. Trajectory 4, in which the SRP is initialized from the *anti* conformation with a bound model SP composed of 14 leucine and alanine residues, is prepared from the coordinates of the 3NDB structure (19). All structures were solvated with explicit water molecules in a orthorhombic simulation cell. Na^+ and Cl^- counterions are added to achieve electroneutrality at a salt concentration of 100 mM for a total size of 168,500 atoms for the SRP in the *syn* conformation and 164,294 atoms for the SRP in the *anti* conformation. Differences in system size are due to different box sizes and different numbers of solvent molecules. Interactions are described by the CHARMM27 force field (72) with TIP3P water.

For each microsecond timescale trajectory, the initial coordinates of the system are equilibrated using the NAMD simulation package (73). Equilibration of the initial configuration consists of conjugate gradient minimization to reduce steric clashes, thermalization of the system to 300 K, and 10 ns of simulation in the NPT ensemble. The system is evolved using Langevin dynamics with a damping constant of 1 ps^{-1}, which also provides temperature control at 300 K. Pressure is maintained at 1 bar using the Nosé-Hoover Langevin piston (74). Long range electrostatics are treated using particle mesh Ewald with a real space cutoff at 12 Å. LJ interactions are switched off between 10 and 12 Å using a cubic spline (73). A 2-fs time step was used throughout, and all bond lengths are constrained using the SHAKE algorithm (75).

Following equilibration, production trajectories were performed on the Anton system. Harmonic restraints are introduced to the phosphate backbone of the SRP RNA with a force constant of 418.4 kJ mol^{-1} $Å^{-2}$ to prevent conformational rearrangements of the SRP RNA domain and to avoid overall rotations of the complex with respect to the simulation cell that might cause interactions with its periodic images. Molecular dynamics are evolved with the RESPA numerical integration scheme with a 2-fs time step (76). The Berendsen coupling scheme maintains the temperature at 300 K and pressure at 1

bar (77). Long range electrostatics are treated using the *k*-space Gaussian Split Ewald method (78) with a real space cutoff of 9.45 Å. LJ interactions were cut off at 9.48 Å. All bond lengths are constrained using the M-SHAKE algorithm (79).

RESULTS AND DISCUSSION

Coupling between SP Binding and SRP Conformation—FEP calculations were used to investigate the potential role of SP binding in driving conformational changes in the SRP. For each SP, we consider $\Delta\Delta G^{(i)}$ as the relative FE of SP binding to the SRP in the *syn versus* the *anti* conformation. As schematically illustrated using the thermodynamic cycle in Fig. 4, we calculate $\Delta\Delta G^{(i)}$ for a given SP *i* using Equation 5,

$$\Delta\Delta G^{(i)} = \Delta G_A^{(i)} - \Delta G_S^{(i)}, \qquad \text{(Eq. 5)}$$

where $\Delta G_A^{(i)}$ and $\Delta G_S^{(i)}$ are the respective binding FE of the SP to the *syn* and *anti* conformations of the SRP. This construction of the thermodynamic cycle avoids the direct calculation of the FE difference between the SRP in the *syn* and *anti* conformation, illustrated by the *horizontal arrows* in Fig. 4.

As explained under "Computational Methods," harmonic restraints are employed in the FE calculations to limit the ensemble of sampled configurations for the SRP to those associated with either the *syn* or *anti* conformations that are observed in the experimental crystal structures (19, 20). We note that a more common implementation of the thermodynamic cycle approach is to first assume that the different conformations of the biomolecule correspond to basins of stability that are separated by a FE barrier and then to fully sample the configuration space associated with those basins of stability. However, well defined FE differences can be computed between any regions of configuration space, and in this study, we focus on calculating the FE differences between configurations in the vicinity of the experimental crystal structure for SRP in the *syn* conformation and configurations in the vicinity of the experimental crystal structure for SRP in the *anti* conformation. The advantages of this approach are 2-fold. (i) It enables us specifically address the effect of SP binding on the relative stability of SRP in its experimentally observed conformations. (ii) By using the restraints to avoid sampling the slow degrees of freedom associated with the flexible linker domain of the SRP, it enables us to rigorously converge all of the reported FE calculations that are reported in this study.

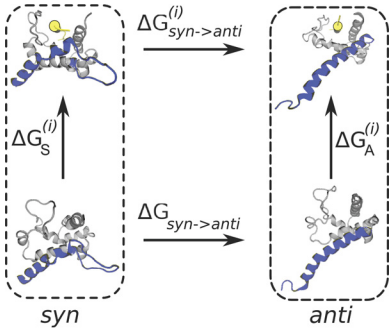

FIGURE 4. **Thermodynamic cycle that enables the quantification of coupling between SP binding and SRP linker conformation.** Four states are defined by linker conformation (*blue*) and the presence or absence of SP (*yellow*). $\Delta\Delta G^{(i)}$ is calculated by taking the difference of $\Delta G_S^{(i)}$ and $\Delta G_A^{(i)}$ in the *dotted boxes*. This is equivalent to the difference of $\Delta G^{(i)}_{syn \rightarrow anti}$ and $\Delta G_{syn \rightarrow anti}$ shown along the *horizontal arrows*.

The primary quantity of interest in this analysis is $\Delta\Delta G^{(i)}$, which reports on the degree to which binding of the SP impacts the conformation of the SRP linker region. The results for the three considered SPs are shown in Table 2. For DPAP-WT, a known targeting sequence, we calculate a value of −11 kJ/mol, which indicates substantial coupling of SP binding to the SRP linker region. Furthermore, the negative sign of $\Delta\Delta G^{(i)}$ for the case of DPAP-WT indicates that SP binding leads to a significant shift in the SRP conformational distribution toward the *anti* conformation, which is consistent with the model hypothesis (Fig. 1*C*).

The computed value of $\Delta\Delta G^{(i)}$ for DPAP-K464L suggests that a single lysine-to-leucine mutation from the DPAP-WT sequence leads to a modest increase in the induced conformational bias in the SRP distribution. The calculated $\Delta\Delta G^{(i)}$ is −16 kJ/mol, which is greater in magnitude than the conformational preference of the DPAP-WT SP, although this difference is within a standard deviation of the statistical error. The DPAP-K464L sequence was chosen because the lysine-to-leucine mutation at residue 464 removes a charged residue and extends the hydrophobic core of the SP. Previous experimental studies (53, 80) have shown that increased hydrophobicity leads to more efficient targeting, and our results are thus consistent with the interpretation that this increased hydrophobicity also leads to a greater conformational preference for the *anti* conformation of the SRP.

Finally, we consider the PhoA SP, which is known to successfully bind to the SRP but which provides inefficient targeting along the co-translational pathway (10, 30, 54). We find (Table 2) that binding of the PhoA SP leads to a reversed shift in the SRP conformational distribution in comparison with DPAP-WT and DPAP-K464L. The calculated $\Delta\Delta G^{(i)}$ is 13 kJ/mol, indicating that binding of PhoA SP stabilizes the *syn* conformation of the SRP relative to the *anti* conformation. This finding is again in agreement with the model hypothesis in which binding of PhoA fails to induce the SRP conformational change that would lead to efficient targeting.

The calculated $\Delta\Delta G^{(i)}$ values demonstrate that SP binding to the SRP is coupled to the linker region, and its effects on the SRP conformational distribution are dependent on the sequence of the SP. For all three considered SPs, the degree to which we find that SP binding induces conformational changes in the SRP is fully consistent with the hypothesis that the SRP targeting path-

TABLE 2
Summary of FE calculation results in units of kJ/mol

i	$\Delta G^{(i)}_{(aq)}$	$\Delta G^{(i)}_{S\ (SRP)}$	$\Delta G^{(i)}_{A\ (SRP)}$	$\Delta G^{(i)}_S$	$\Delta G^{(i)}_A$	$\Delta\Delta G^{(i)}$
DPAP-WT	−310 (2)	−389 (2)	−400 (3)	−79 (3)	−90 (3)	−11 (4)
DPAP-K464L	−275 (2)	−340 (2)	−355 (2)	−65 (3)	−80 (3)	−16 (7)
PhoA	−287 (2)	−326 (2)	−314 (2)	−39 (3)	−27 (3)	13 (4)

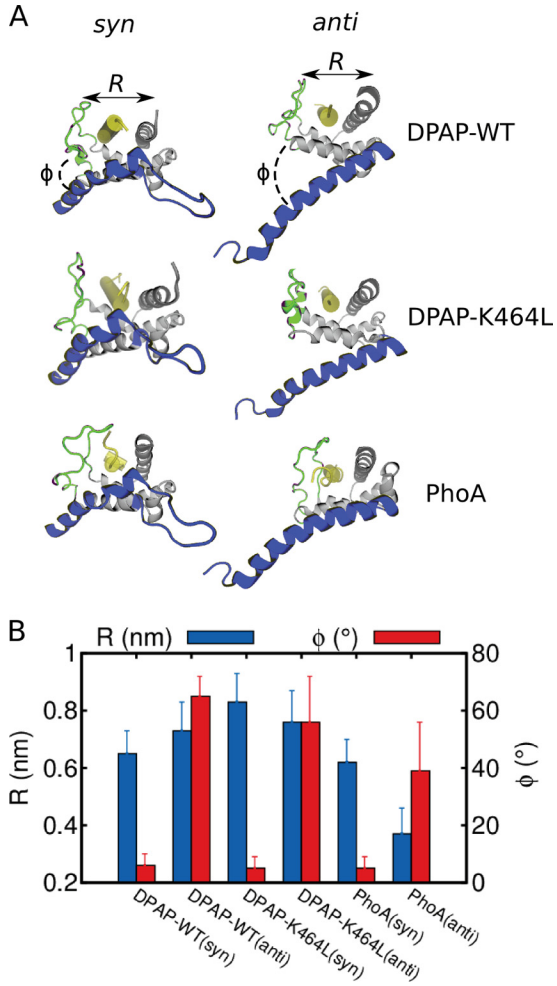

FIGURE 5. *A*, ensemble-averaged structures from SP-bound sampling trajectories with the linker region shown in *blue*, the fingerloop shown in *green*, and the SP shown in *yellow*. *B*, fingerloop displacement *R* and the relative orientation of the linker and αM1 helix ϕ are shown for each SP and SRP pair, revealing the structural differences associated with binding efficient and inefficient SPs.

way is triggered by SP binding that induces conformational changes in the SRP from the *syn* to the *anti* conformation. Furthermore, the results explain the counter-intuitive experimental observation that SPs with favorable binding to the SRP need not lead to efficient downstream protein targeting (41); indeed, it is seen here that favorable PhoA binding induces a shift toward the *syn* conformation of SRP, which hinders the kinetics of complex formation between SRP and its receptor. We additionally note that this connection between SRP conformational shifts upon substrate binding provides a mechanism for SP identity to influence the kinetics of processes at large distances from the SP-binding site.

FE calculations not only provide a quantitative measure of the extent of allosteric coupling between SP binding and SRP linker conformation, but the sampling trajectories also provide details of the structural differences in the SRP upon binding of the different SPs. For each SP considered, Fig. 5*A* shows the ensemble-averaged configuration of the SRP in the *syn* and *anti* conformations. In each case, the fingerloop of the SRP reorganizes to accommodate binding of the SP. The position of the fingerloop, measured in terms of its center-of-mass distance *R* from the fifth helix of the M domain (αM5) helix at the opposite side of the SP binding pocket, is found to be displaced by 4–9 Å upon SP binding (Fig. 5*A*). This is in agreement with previous structural and biochemical work (28, 40), which suggests that SP binding displaces the fingerloop and that fingerloop flexibility is crucial for enabling the SRP to bind to SPs of differing sequences.

The three SPs considered here differ substantially in terms of their size, with DPAP-WT and DPAP-K464L excluding more volume than PhoA (Table 1). These differences are reflected in the conformation of the SRP bound to the SP, in terms of both the degree of fingerloop displacement and the relative orientation between the linker region and M domain. These conformational differences are shown in Fig. 5*B*, where the relative orientation is monitored by the dihedral angle ϕ between the helical axis of the linker and the axis of the first helix of the M domain (αM1), as well as by the fingerloop displacement, *R*. For each SP, the observed dihedral angle associated with binding in the *syn* conformation is small. For the cases of DPAP-WT and DPAP-K464L bound to the SRP in the *anti* conformation, the value of ϕ is much larger than in the *syn* conformation due to the loss of contact between the linker and the M domain; the smaller PhoA SP likewise exhibits an increased value of ϕ in the *anti* conformation but to a lesser extent. A more striking trend is observed in the fingerloop displacement, *R*. For both of the efficiently targeted sequences, DPAP-WT and DPAP-K464L, the fingerloop is substantially displaced in both the *syn* and *anti* conformations, whereas the inefficiently targeted PhoA SP exhibits a reduced displacement of the fingerloop in the *anti* conformation. The differing degree to which the efficient and inefficient SPs impact these structural features of the SRP suggests a mechanistic basis for the observed correlations between SP binding and SRP conformational changes (Table 2). Although the single amino acid mutation that distinguishes the DPAP-WT and DPAP-K464L SPs appears to have a relatively small impact on the corresponding values of $\Delta\Delta G^{(i)}$ (Table 2), and although the binding of these two SPs leads to similar structural changes in the SRP fingerloop displacement and helix orientation (Fig. 5*B*), we do note that the binding of these two SPs leads to differences in other structural quantities. In DPAP-WT, the positive charge interacts with the negatively charged residues of the fingerloop (Asp-364 and Glu-365) in the *syn* conformation, but this interaction is not observed in the *anti* conformation; the DPAP-K464L mutant lacks the positive charge for this interaction with the *syn* conformation. These different interactions may explain the somewhat stronger bias of the DPAP-K464L mutant for the *anti* conformation of the SRP upon binding. Regardless, these results illustrate that specific amino acid interactions can play a role in determining the conformational shift of the SRP upon SP binding.

Large Scale Conformational Changes from Microsecond Trajectories—Microsecond trajectories are performed with the Anton supercomputer (70) to investigate the conformational dynamics of the SRP (Table 3). Fig. 6 plots the fingerloop displacement, *R*, and the dihedral angle between the helical axis of the linker and αM1 helix, ϕ, as a function of simulation time for all four trajectories; these geometric quantities were previously introduced in the discussion of the FE sampling trajecto-

TABLE 3
Summary of microsecond trajectories

Trajectory	Initial SRP configuration	SP	Time
			μs
T1	*syn*	No SP	3.6
T2	*syn*	With SP	4.5
T3	*anti*	No SP	4.3
T4	*anti*	With SP	3.4

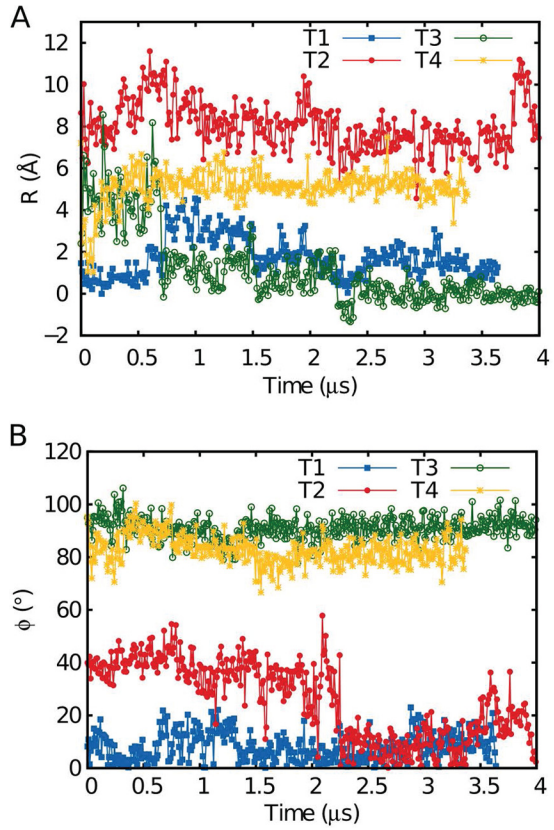

FIGURE 6. *A*, fingerloop displacement *R* as a function of time in the microsecond timescale MD trajectories. *B*, relative orientation of the linker and αM1 helix ϕ as a function of time in the microsecond timescale MD trajectories.

ries that involved the truncated SRP system (Fig. 5). Comparison of Figs. 5 and 6 reveals similar structural responses of the SRP to binding of the various SPs, confirming that *R* and ϕ are relatively local geometric features that are unchanged by inclusion of the NG domain. For trajectories T1 and T3, neither of which include the bound SP, it is seen in Fig. 6*A* that the fingerloop occludes the binding pocket, exhibiting a small value for the displacement distance. For trajectories T2 and T4, both of which include the bound SP, it is seen that the fingerloop is significantly displaced (4–9 Å) to accommodate the SP; these results are consistent with the observations in Fig. 5 that SP binding displaces the fingerloop from the binding pocket. Similarly, for trajectories T1 and T2, both of which are initialized in the *syn* conformation, it is seen in Fig. 6*B* that the SRP undergoes relaxation to adopt configurations with values of ϕ that are consistent with those observed in the equilibrium FE sampling trajectories for SRP in the *syn* conformation (Fig. 5). For trajectories T3 and T4, both of which are initialized in the *anti* conformation, it is seen in Fig. 6*B* that the SRP adopts configurations with values of ϕ that are consistent with the loss of contact between the linker region and the M domain, which is again consistent with the structural features that are observed for the equilibrium FE sampling trajectories for SRP in the *anti* conformation (Fig. 5).

To further characterize the conformational changes observed in the microsecond timescale MD trajectories, Fig. 7 shows snapshots of the system at various times along the trajectories. In addition to illustrating the changes in *R* and ϕ that were discussed previously, Fig. 7 also illustrates the process by which the fingerloop collapses to occupy the SRP binding pocket in the absence of the bound SP (trajectory T3).

We now analyze the microsecond timescale MD trajectories in the context of a recent study by Shen *et al.* (16), which used single molecule FRET experiments to monitor the SRP conformational dynamics. This experimental study labeled the SRP RNA distal end and NG domain and found that the SRP samples both a low efficiency and a high efficiency FRET state, with differences in FRET efficiency that correspond to distance changes of ~10 nm. Fig. 8 presents results from the four microsecond timescale MD simulations of the SRP, plotting the distance between the G domain and RNA corresponding to the donor-acceptor distance measured in the single molecule FRET experiments. Trajectories T1 and T2, which are initialized from the *syn* conformation of the SRP, show 6–8 nm changes in donor-acceptor distance during the course of the simulation. Trajectory T2, which has a bound SP, has greater fluctuations in this coordinate than T1, which does not have a bound SP. Trajectories T3 and T4, which are initialized from the *anti* conformation of the SRP, exhibit little deviation from the initial distance. These results support the conclusion that nanometer-length scale changes in SRP conformation are intrinsic features of the SRP, although we do not suggest that the conformational states observed in these trajectories correspond directly to the low-FRET and high-FRET states reported by Shen *et al.* (16).

Interestingly, the trajectories reveal that nanometer-length scale changes in distance occur via the rigid-body movement of M and NG domains connected by the flexible linker region, although the conformation of each individual domain is unchanged. In Fig. 9*A*, for each residue pair *i* and *j* in the SRP, we plot $\delta_{ij}(t) = |d_{ij}(0) - d_{ij}(t)|$, the difference in the distance d_{ij} between the two Cα atoms of each residue at the initial configuration of the trajectory and at various subsequent times *t* along trajectory T2. This metric reveals only small changes in distance between atom pairs that both belong to the M domain or that both belong to the NG domain, which correspond to the indicated diagonal blocks in Fig. 9*A*. Large distance changes are only observed in atom pairs for which one atom is in the M domain and the other is in the NG domain, which correspond to the off-diagonal blocks. This suggests that the observed changes in conformation and donor-acceptor distance are the result of changes in the relative orientation of the M and NG domains, whereas the M and NG domains individually evolve as rigid bodies. Fig. 9*B* further illustrates this point by plotting the average of δ_{ij} over NG-NG pairs, M-M pairs, and M-NG pairs along the trajectory. It is clear that only the M and NG domains undergo large changes in relative orientation in trajectory T2.

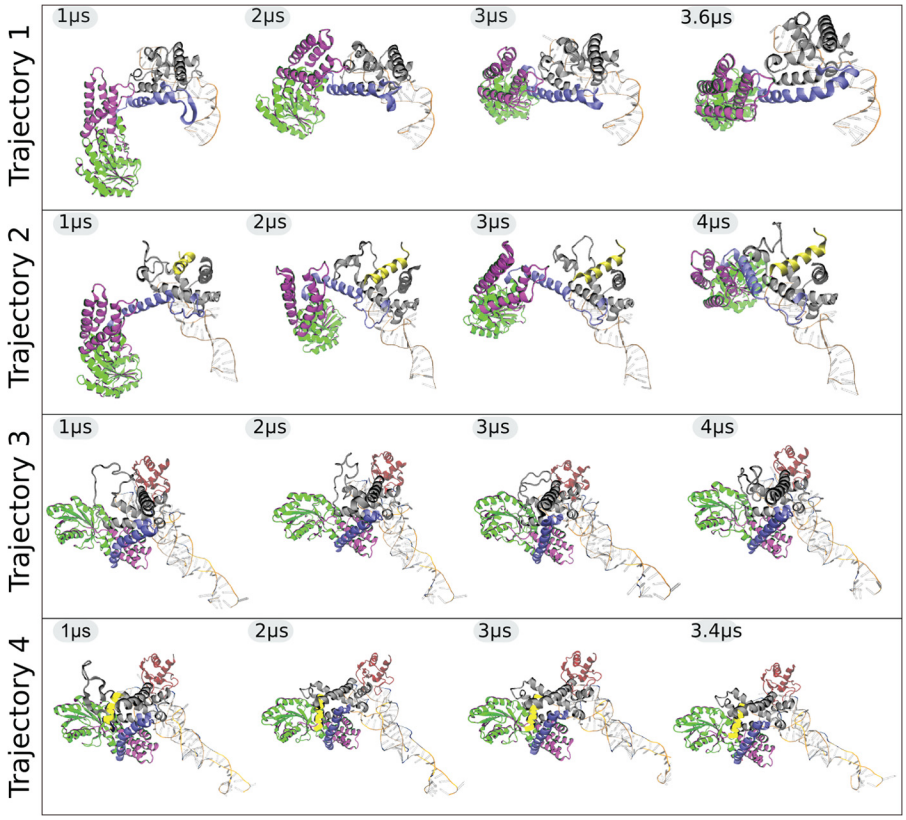

FIGURE 7. **Snapshots of full-system SRP trajectories shown at microsecond intervals.** All structures were aligned by the SRP RNA, shown in *orange*, with M domain, linker region, N and G domain shown in *gray, blue, purple,* and *green*, respectively. Trajectories T2 and T4 have bound SP shown in *yellow*.

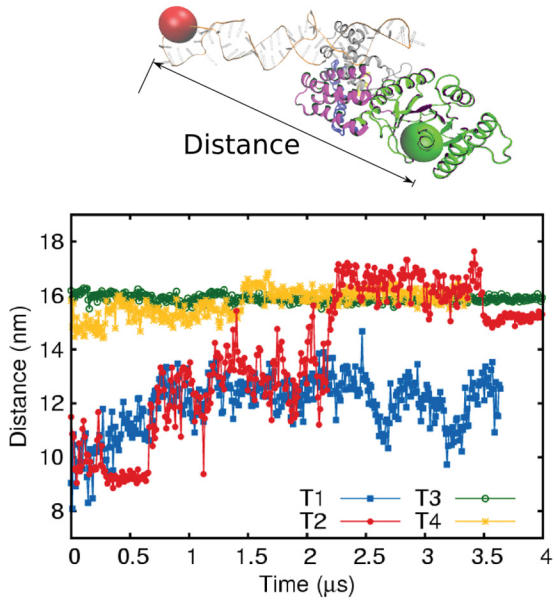

FIGURE 8. **Distance between the FRET donor (*green*) and acceptor (*red*) positions as a function of time in the microsecond timescale MD trajectories.**

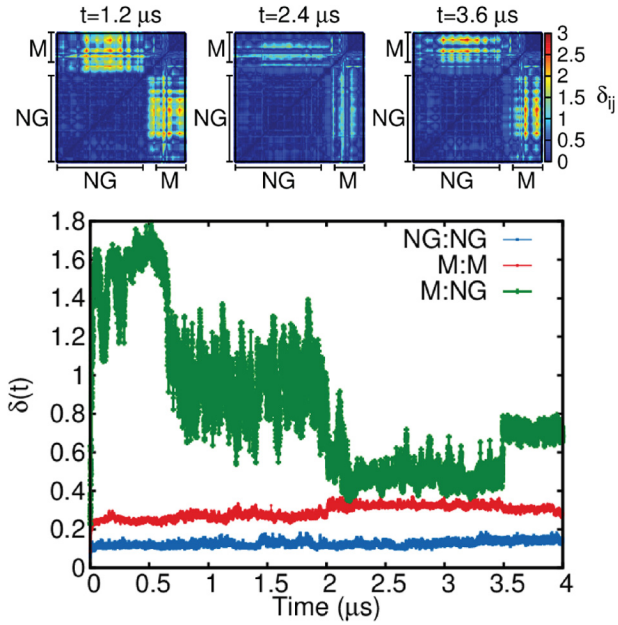

FIGURE 9. *A,* for each residue pair *i* and *j* in the SRP, the difference in the distance δ_{ij} between the two Cα atoms of each residue at the initial configuration of the trajectory and at various subsequent times along trajectory T2. *B,* average of δ_{ij} over NG-NG pairs, M-M pairs, and M-NG pairs.

The same conclusion holds for the other microsecond trajectories that were performed in this study.

The microsecond timescale dynamics revealed in these simulations suggest a mechanism for coordinating the spatial and temporal organization between independent functional domains. In SRP, SP binding occurs in the M domain, and downstream targeting events, such as dimerization of the SRP with its receptor and GTPase activity of the SRP, involve the NG domain of the SRP (81). From the earlier FE simulations (Fig. 4 and Table 2), it is evident that SP binding leads to sequence-specific changes in the conformational distribution in the flexible linker domain. Fig. 9 further reveals that such changes in the linker domain

manifest as large lengthscale changes in the relative orientation of the M and NG domains of the SRP, thus coordinating SP binding at the M domain with downstream steps involving the NG domain.

Conclusions—The fidelity of co-translational protein targeting and recognition is a remarkable feature of cellular signaling pathways that demands understanding from the perspective of molecular interactions. The central component of co-translational targeting, the SRP, is capable of binding a diverse set of SPs while differentiating between sequences with similar biochemical features. In this work, we have demonstrated allosteric coupling between SP binding and conformational changes of the linker region of the SRP. This coupling is sensitive to the sequence identity of the SP, thus providing a mechanism for conferring SP sequence specificity in the signaling pathway. Furthermore, microsecond timescale simulations reveal that the SRP undergoes large scale conformational changes that are characterized by rigid body motion of individual domains connected by a flexible linker, which enables small conformational changes of the linker upon SP binding to be conferred onto larger ~10-nm lengthscales.

Acknowledgments—Computational resources were provided by the National Energy Research Scientific Computing Center, which is supported by the Office of Science of the United States Department of Energy under Contract DE-AC02-05CH11231. Additionally, Anton computer time was provided by the National Resource for Biomedical Supercomputing, the Pittsburgh Supercomputing Center, and the Biomedical Technology Research Center for Multiscale Modeling of Biological Systems through National Institutes of Health Grant P41GM103712-S1. The Anton machine at NRBSC/PSC was generously made available by D. E. Shaw Research. We also thank Shu-ou Shan and David Akopian for helpful discussions.

REFERENCES

1. Akopian, D., Shen, K., Zhang, X., and Shan, S. O. (2013) Signal recognition particle: an essential protein-targeting machine. *Annu. Rev. Biochem.* **82,** 693–721
2. Pohlschröder, M., Prinz, W. A., Hartmann, E., and Beckwith, J. (1997) Protein translocation in the three domains of life: variations on a theme. *Cell* **91,** 563–566
3. Walter, P., Ibrahimi, I., and Blobel, G. (1981) Translocation of proteins across the endoplasmic reticulum. 1. Signal recognition protein (SRP) binds to *in vitro*-assembled polysomes synthesizing secretory protein. *J. Cell Biol.* **91,** 545–550
4. Rapoport, T. A., Jungnickel, B., and Kutay, U. (1996) Protein transport across the eukaryotic endoplasmic reticulum and bacterial inner membranes. *Annu. Rev. Biochem.* **65,** 271–303
5. Powers, T., and Walter, P. (1997) Co-translational protein targeting catalyzed by the *Escherichia coli* signal recognition particle and its receptor. *EMBO J.* **16,** 4880–4886
6. Rapoport, T. A. (2007) Protein translocation across the eukaryotic endoplasmic reticulum and bacterial plasma membranes. *Nature* **450,** 663–669
7. Driessen, A. J., and Nouwen, N. (2008) Protein translocation across the bacterial cytoplasmic membrane. *Annu. Rev. Biochem.* **77,** 643–667
8. Zhang, B., and Miller, T. F., 3rd (2012) Direct simulation of early-stage Sec-facilitated protein translocation. *J. Am. Chem. Soc.* **134,** 13700–13707
9. Zhang, B., and Miller, T. F., 3rd (2012) Long-timescale dynamics and regulation of Sec-facilitated protein translocation. *Cell Rep.* **2,** 927–937
10. Gierasch, L. M. (1989) Signal sequences. *Biochemistry* **28,** 923–930
11. von Heijne, G. (1985) Signal sequences–the limits of variation. *J. Mol. Biol.* **184,** 99–105
12. Halic, M., Blau, M., Becker, T., Mielke, T., Pool, M. R., Wild, K., Sinning, I., and Beckmann, R. (2006) Following the signal sequence from ribosomal tunnel exit to signal recognition particle. *Nature* **444,** 507–511
13. Schaffitzel, C., Oswald, M., Berger, I., Ishikawa, T., Abrahams, J. P., Koerten, H. K., Koning, R. I., and Ban, N. (2006) Structure of the *E-coli* signal recognition particle bound to a translating ribosome. *Nature* **444,** 503–506
14. Estrozi, L. F., Boehringer, D., Shan, S. O., Ban, N., and Schaffitzel, C. (2011) Cryo-EM structure of the *E. coli* translating ribosome in complex with SRP and its receptor. *Nat. Struct. Mol. Biol.* **18,** 88–90
15. Holtkamp, W., Lee, S., Bornemann, T., Senyushkina, T., Rodnina, M. V., and Wintermeyer, W. (2012) Dynamic switch of the signal recognition particle from scanning to targeting. *Nat. Struct. Mol. Biol.* **19,** 1332–1337
16. Shen, K., Arslan, S., Akopian, D., Ha, T., and Shan, S. O. (2012) Activated GTPase movement on an RNA scaffold drives co-translational protein targeting. *Nature* **492,** 271–275
17. Janda, C. Y., Li, J., Oubridge, C., Hernández, H., Robinson, C. V., and Nagai, K. (2010) Recognition of a signal peptide by the signal recognition particle. *Nature* **465,** 507–510
18. Hainzl, T., Huang, S., and Sauer-Eriksson, A. E. (2007) Interaction of signal-recognition particle 54 GTPase domain and signal-recognition particle RNA in the free signal-recognition particle. *Proc. Natl. Acad. Sci. U.S.A.* **104,** 14911–14916
19. Hainzl, T., Huang, S., Meriläinen, G., Brännström, K., and Sauer-Eriksson, A. E. (2011) Structural basis of signal-sequence recognition by the signal recognition particle. *Nat. Struct. Mol. Biol.* **18,** 389–391
20. Rosendal, K. R., Wild, K., Montoya, G., and Sinning, I. (2003) Crystal structure of the complete core of archaeal signal recognition particle and implications for interdomain communication. *Proc. Natl. Acad. Sci. U.S.A.* **100,** 14701–14706
21. Ataide, S. F., Schmitz, N., Shen, K., Ke, A., Shan, S. O., Doudna, J. A., and Ban, N. (2011) The crystal structure of the signal recognition particle in complex with its receptor. *Science* **331,** 881–886
22. Wild, K., Rosendal, K. R., and Sinning, I. (2004) A structural step into the SRP cycle. *Mol. Microbiol.* **53,** 357–363
23. Wild, K., Bange, G., Bozkurt, G., Segnitz, B., Hendricks, A., and Sinning, I. (2010) Structural insights into the assembly of the human and archaeal signal recognition particles. *Acta Crystallogr. D Biol. Crystallogr.* **66,** 295–303
24. Noriega, T. R., Tsai, A., Elvekrog, M. M., Petrov, A., Neher, S. B., Chen, J., Bradshaw, N., Puglisi, J. D., and Walter, P. (2014) Signal recognition particle-ribosome binding is sensitive to nascent-chain length. *J. Biol. Chem.* **289,** 19294–19305
25. Kurzchalia, T. V., Wiedmann, M., Girshovich, A. S., Bochkareva, E. S., Bielka, H., and Rapoport, T. A. (1986) The signal sequence of nascent preprolactin interacts with the 54K polypeptide of the signal recognition particle. *Nature* **320,** 634–636
26. Poritz, M. A., Bernstein, H. D., Strub, K., Zopf, D., Wilhelm, H., and Walter, P. (1990) An *E. coli* ribonucleoprotein containing 4.5 S RNA resembles mammalian signal recognition particle. *Science* **250,** 1111–1117
27. Freymann, D. M., Keenan, R. J., Stroud, R. M., and Walter, P. (1997) Structure of the conserved GTPase domain of the signal recognition particle. *Nature* **385,** 361–364
28. Keenan, R. J., Freymann, D. M., Walter, P., and Stroud, R. M. (1998) Crystal structure of the signal sequence binding subunit of the signal recognition particle. *Cell* **94,** 181–191
29. Batey, R. T., Rambo, R. P., Lucast, L., Rha, B., and Doudna, J. A. (2000) Crystal structure of the ribonucleoprotein core of the signal recognition particle. *Science* **287,** 1232–1239
30. Zhang, X., Rashid, R., Wang, K., and Shan, S. O. (2010) Sequential checkpoints govern substrate selection during cotranslational protein targeting. *Science* **328,** 757–760
31. Egea, P. F., Stroud, R. M., and Walter, P. (2005) Targeting proteins to membranes: structure of the signal recognition particle. *Curr. Opin. Struct. Biol.* **15,** 213–220
32. Focia, P. J., Shepotinovskaya, I. V., Seidler, J. A., and Freymann, D. M. (2004) Heterodimeric GTPase core of the SRP targeting complex. *Science* **303,** 373–377

33. Peluso, P., Shan, S. O., Nock, S., Herschlag, D., and Walter, P. (2001) Role of SRP RNA in the GTPase cycles of Ffh and FtsY. *Biochemistry* **40,** 15224–15233
34. Siu, F. Y., Spanggord, R. J., and Doudna, J. A. (2007) SRP RNA provides the physiologically essential GTPase activation function in cotranslational protein targeting. *RNA* **13,** 240–250
35. Bradshaw, N., Neher, S. B., Booth, D. S., and Walter, P. (2009) Signal sequences activate the catalytic switch of SRP RNA. *Science* **323,** 127–130
36. Zhang, X., Schaffitzel, C., Ban, N., and Shan, S. O. (2009) Multiple conformational switches in a GTPase complex control co-translational protein targeting. *Proc. Natl. Acad. Sci. U.S.A.* **106,** 1754–1759
37. Zhang, X., Lam, V. Q., Mou, Y., Kimura, T., Chung, J., Chandrasekar, S., Winkler, J. R., Mayo, S. L., and Shan, S. O. (2011) Direct visualization reveals dynamics of a transient intermediate during protein assembly. *Proc. Natl. Acad. Sci. U.S.A.* **108,** 6450–6455
38. Shen, K., Zhang, X., and Shan, S. O. (2011) Synergistic actions between the SRP RNA and translating ribosome allow efficient delivery of the correct cargos during cotranslational protein targeting. *RNA* **17,** 892–902
39. von Loeffelholz, O., Knoops, K., Ariosa, A., Zhang, X., Karuppasamy, M., Huard, K., Schoehn, G., Berger, I., Shan, S. O., and Schaffitzel, C. (2013) Structural basis of signal sequence surveillance and selection by the SRP-FtsY complex. *Nat. Struct. Mol. Biol.* **20,** 604–610
40. Ariosa, A. R., Duncan, S. S., Saraogi, I., Lu, X., Brown, A., Phillips, G. J., and Shan, S. O. (2013) Fingerloop activates cargo delivery and unloading during cotranslational protein targeting. *Mol. Biol. Cell* **24,** 63–73
41. Saraogi, I., Akopian, D., and Shan, S. O. (2014) Regulation of cargo recognition, commitment, and unloading drives cotranslational protein targeting. *J. Cell Biol.* **205,** 693–706
42. Jorgensen, W. L., and Ravimohan, C. (1985) Monte Carlo simulation of differences in free energies of hydration. *J. Chem. Phys.* **83,** 3050–3054
43. Bash, P. A., Singh, U. C., Langridge, R., and Kollman, P. A. (1987) Free energy calculations by computer simulation. *Science* **236,** 564–568
44. Rao, S. N., Singh, U. C., Bash, P. A., and Kollman, P. A. (1987) Free energy perturbation calculations on binding and catalysis after mutating Asn 155 in subtilisin. *Nature* **328,** 551–554
45. Roux, B., Nina, M., Pomès, R., and Smith, J. (1996) Thermodynamic stability of water molecules in the bacteriorhodopsin proton channel: a molecular dynamics free energy perturbation study. *Biophys. J.* **71,** 670–681
46. Essex, J. W., Severance, D. L., Tirado-Rives, J., and Jorgensen, W. L. (1997) Monte Carlo simulations for proteins: binding affinities for trypsin-benzamidine complexes via free-energy perturbations. *J. Phys. Chem. B* **101,** 9663–9669
47. Woo, H.-J., and Roux, B. (2005) Calculation of absolute protein–ligand binding free energy from computer simulations. *Proc. Natl. Acad. Sci. U.S.A.* **102,** 6825–6830
48. Jayaram, B., Sprous, D., Young, M. A., and Beveridge, D. L. (1998) Free energy analysis of the conformational preferences of A and B forms of DNA in solution. *J. Am. Chem. Soc.* **120,** 10629–10633
49. Satpati, P., Clavaguéra, C., Ohanessian, G., and Simonson, T. (2011) Free energy Simulations of a GTPase: GTP and GDP binding to archaeal initiation factor 2. *J. Phys. Chem. B* **115,** 6749–6763
50. Larkin, M. A., Blackshields, G., Brown, N. P., Chenna, R., McGettigan, P. A., McWilliam, H., Valentin, F., Wallace, I. M., Wilm, A., Lopez, R., Thompson, J. D., Gibson, T. J., and Higgins, D. G. (2007) Clustal W and Clustal X version 2.0. *Bioinformatics* **23,** 2947–2948
51. Eswar, N., Webb, B., Marti-Renom, M. A., Madhusudhan, M., Eramian, D., Shen, M.-Y., Pieper, U., and Sali, A. (2006) Comparative protein structure modeling using modeller. *Curr. Protoc. Bioinformatics.* 2006 Chapter 5, Unit 5.6
52. MacKerell, A. D., Bashford, D., Bellott, M., Dunbrack, R. L., Evanseck, J. D., Field, M. J., Fischer, S., Gao, J., Guo, H., Ha, S., Joseph-McCarthy, D., Kuchnir, L., Kuczera, K., Lau, F. T., Mattos, C., Michnick, S., Ngo, T., Nguyen, D. T., Prodhom, B., Reiher, W. E., Roux, B., Schlenkrich, M., Smith, J. C., Stote, R., Straub, J., Watanabe, M., Wiórkiewicz-Kuczera, J., Yin, D., and Karplus, M. (1998) All-atom empirical potential for molecular modeling and dynamics studies of proteins. *J. Phys. Chem. B* **102,** 3586–3616
53. Ng, D. T., Brown, J. D., and Walter, P. (1996) Signal sequences specify the targeting route to the endoplasmic reticulum membrane. *J. Cell Biol.* **134,** 269–278
54. Huber, D., Boyd, D., Xia, Y., Olma, M. H., Gerstein, M., and Beckwith, J. (2005) Use of thioredoxin as a reporter to identify a subset of *Escherichia coli* signal sequences that promote signal recognition particle-dependent translocation. *J. Bacteriol.* **187,** 2983–2991
55. Fletcher, R., and Powell, M. J. D. (1963) A rapidly convergent descent method for minimization. *Comput. J.* **6,** 163–168
56. Beutler, T. C., Mark, A. E., van Schaik, R. C., Gerber, P. R., and van Gunsteren, W. F. (1994) Avoiding singularities and numerical instabilities in free energy calculations based on molecular simulations. *Chem. Phys. Lett.* **222,** 529–539
57. Steinbrecher, T., Mobley, D. L., and Case, D. A. (2007) Nonlinear scaling schemes for Lennard-Jones interactions in free energy calculations. *J. Chem. Phys.* **127,** 214108
58. Hess, B., Kutzner, C., van der Spoel, D., and Lindahl, E. (2008) GROMACS 4: Algorithms for highly efficient, load-balanced, and scalable molecular simulation. *J. Chem. Theory Comput.* **4,** 435–447
59. Duan, Y., Wu, C., Chowdhury, S., Lee, M. C., Xiong, G., Zhang, W., Yang, R., Cieplak, P., Luo, R., Lee, T., Caldwell, J., Wang, J., and Kollman, P. (2003) A point-charge force field for molecular mechanics simulations of proteins based on condensed-phase quantum mechanical calculations. *J. Comput. Chem.* **24,** 1999–2012
60. Jorgensen, W. L., Chandrasekhar, J., Madura, J. D., Impey, R. W., and Klein, M. L. (1983) Comparison of simple potential functions for simulating liquid water. *J. Chem. Phys.* **79,** 926–935
61. Bonomi, M., Branduardi, D., Bussi, G., Camilloni, C., Provasi, D., Raiteri, P., Donadio, D., Marinelli, F., Pietrucci, F., Broglia, R. A., and Parrinello, M. (2009) PLUMED: A portable plugin for free-energy calculations with molecular dynamics. *Comput. Phys. Comm.* **180,** 1961–1972
62. Parrinello, M., and Rahman, A. (1981) Polymorphic transitions in single crystals: A new molecular dynamics method. *J. Appl. Phys.* **52,** 7182–7190
63. Darden, T., York, D., and Pedersen, L. (1993) Particle mesh Ewald: An *N* log (*N*) method for Ewald sums in large systems. *J. Chem. Phys.* **98,** 10089–10092
64. Essmann, U., Perera, L., Berkowitz, M. L., Darden, T., Lee, H., and Pedersen, L. G. (1995) A smooth particle mesh Ewald method. *J. Chem. Phys.* **103,** 8577–8593
65. van Gunsteren, W. F., and Berendsen, H. J. (1990) Computer simulation of molecular dynamics: methodology, applications, and perspectives in chemistry. *Angew. Chem. Int. Ed. Engl.* **29,** 992–1023
66. Bennett, C. H. (1976) Efficient estimation of free-energy differences from Monte-Carlo data. *J. Comput. Phys.* **22,** 245–268
67. Pohorille, A., Jarzynski, C., and Chipot, C. (2010) Good practices in free-energy calculations. *J. Phys. Chem. B* **114,** 10235–10253
68. Lin, Y.-L., Aleksandrov, A., Simonson, T., and Roux, B. (2014) An overview of electrostatic free energy computations for solutions and proteins. *J. Chem. Theory Comput.* **10,** 2690–2709
69. Rocchia, W., Alexov, E., and Honig, B. (2001) Extending the applicability of the nonlinear Poisson Boltzmann equation: multiple dielectric constants and multivalent ions. *J. Phys. Chem. B* **105,** 6507–6514
70. Shaw, D. E., Deneroff, M. M., Dror, R. O., Kuskin, J. S., Larson, R. H., Salmon, J. K., Young, C., Batson, B., Bowers, K. J., Chao, J. C., Eastwood, M. P., Gagliardo, J., Grossman, J. P., Ho, C. R., Ierardi, D. J., Klepeis, J. L., Layman, T., McLeavey, C., Moraes, M. A., Mueller, R., Priest, E. C., Shan, Y., Spengler, J., Theobald, M., Towles, B., and Wang, S. C. (2007) Anton, a special-purpose machine for molecular dynamics simulation. *SIGARCH Comput. Archit. News* **35,** 1–12
71. Shaw, D., Dror, R., Salmon, J., Grossman, J., Mackenzie, K., Bank, J., Young, C., Deneroff, M., Batson, B., Bowers, K., Chow, E., Eastwood, M., Ierardi, D., Klepeis, J., Kuskin, J., Larson, R., Lindorff-Larsen, K., Maragakis, P., Moraes, M., Piana, S., Shan, Y., and Towles, B. (2009) in *Proceedings of the Conference on High Performance Computing Networking, Storage and Analysis,* New York 2009, pp. 1–11, Association of Computer Machinery, New York
72. Foloppe, N., and MacKerell, A. D., Jr. (2000) All-atom empirical force field for nucleic acids: I. Parameter optimization based on small molecule and condensed phase macromolecular target data. *J. Comput. Chem.* **21,**

86–104
73. Phillips, J. C., Braun, R., Wang, W., Gumbart, J., Tajkhorshid, E., Villa, E., Chipot, C., Skeel, R. D., Kalé, L., and Schulten, K. (2005) Scalable molecular dynamics with NAMD. *J. Comput. Chem.* **26,** 1781–1802
74. Feller, S. E., Zhang, Y., Pastor, R. W., and Brooks, B. R. (1995) Constant pressure molecular dynamics simulation–the Langevin piston method. *J. Chem. Phys.* **103,** 4613–4621
75. Ryckaert, J.-P., Ciccotti, G., and Berendsen, H. J. C. (1977) Numerical integration of the cartesian equations of motion of a system with constraints: molecular dynamics of *n*-alkanes. *J. Comput. Phys.* **23,** 327–341
76. Tuckerman, M., Berne, B. J., and Martyna, G. J. (1992) Reversible multiple timescale molecular dynamics. *J. Chem. Phys.* **97,** 1990–2001
77. Berendsen, H. J. C., Postma, J. P. M., van Gunsteren, W. F., DiNola, A., and Haak, J. (1984) Molecular dynamics with coupling to an external bath. *J. Chem. Phys.* **81,** 3684–3690
78. Shan, Y., Klepeis, J. L., Eastwood, M. P., Dror, R. O., and Shaw, D. E. (2005) Gaussian split Ewald: A fast Ewald mesh method for molecular simulation. *J. Chem. Phys.* **122,** 054101
79. Kräutler, V., van Gunsteren, W. F., and Hünenberger, P. H. (2001) A fast SHAKE algorithm to solve distance constraint equations for small molecules in molecular dynamics simulations. *J. Comput. Chem.* **22,** 501–508
80. Hatsuzawa, K., Tagaya, M., and Mizushima, S. (1997) The hydrophobic region of signal peptides is a determinant for SRP recognition and protein translocation across the ER membrane. *J. Biochem.* **121,** 270–277
81. Egea, P. F., Shan, S. O., Napetschnig, J., Savage, D. F., Walter, P., and Stroud, R. M. (2004) Substrate twinning activates the signal recognition particle and its receptor. *Nature* **427,** 215–221
82. Humphrey, W., Dalke, A., and Schulten, K. (1996) VMD: Visual molecular dynamics. *J. Mol. Graphics* **14,** 33–38